Physics of Fluids

Structural variations of endothelial cell monolayer under startup shear conditions

Cite as: Phys. Fluids **35**, 021902 (2023); https://doi.org/10.1063/5.0136707
Submitted: 28 November 2022 • Accepted: 13 January 2023 • Accepted Manuscript Online: 13 January 2023 • Published Online: 02 February 2023

Konstantina Psaraki, Vlasios Mitsoulas, Stavros Pavlou, et al.

Physics of Fluids ARTICLE scitation.org/journal/phf

Structural variations of endothelial cell monolayer under startup shear conditions

Cite as: Phys. Fluids **35**, 021902 (2023); doi: 10.1063/5.0136707
Submitted: 28 November 2022 · Accepted: 13 January 2023 ·
Published Online: 2 February 2023

View Online Export Citation CrossMark

Konstantina Psaraki, Vlasios Mitsoulas,[a] Stavros Pavlou, and Yannis Dimakopoulos[b]

AFFILIATIONS

Laboratory of Fluid Mechanics and Rheology, Department of Chemical Engineering, University of Patras, Patras, Greece

[a]**Current address:** Haute école d'ingénierie et d'architecture de Fribourg, HES-SO Fribourg, Fribourg, Switzerland.
[b]**Author to whom correspondence should be addressed:** dimako@chemeng.upatras.gr

ABSTRACT

We study the response of an endothelial cell monolayer lining the bottom surface of a cartesian Couette geometry in variations of critical shearing parameters that affect the fluid environment, such as the gap distance between the upper moving and the bottom stationary plates and the velocity of the moving plate. Specifically, we propose an *in silico* rheometric emulation based on startup shear experiments in a representative two-dimensional domain of the monolayer that accounts for the interaction of the blood plasma and the deformable multilayer poroelastic endothelial cells. We present quantitative predictions for the shear and normal stresses on each cell compartment (membrane, cytoplasm, and nucleus) and their structural changes. We show that the variation of the Wall Shear Stress (WSS) along the cell membrane is considered significant and strongly dependent on the shape of the cell, while membrane thinning is more prominent at the locus of high WSS in the range of physiological velocities. However, under extreme velocities, wall thinning prevails at the locus of flow stagnation.

I. INTRODUCTION

Blood vessels are typically composed of three distinct layers: the intima, the media, and the adventitia.[1] The innermost layer of intima, which is the region that concerns us in this work, is the thinnest constituent structure and consists of a monolayer of endothelial cells (ECs) that are mounted on the tissue membrane (*basal lamina*).[2] The endothelial cell monolayer (ECM) is recognized, apart from its role as a barrier, to be a predominant player in the control of blood fluidity,[3] vascular tone,[4] a major factor in the regulation of immunology,[5] inflammation,[3] and a metabolizing and endocrine organ.[5] Apparently, the role of the mechanical forces exerted on it is crucial for its homeostasis and is related to the hemodynamics and the shape of the vessel.[6] Because of the corrugated shape of the ECM, different parts of the membrane of an EC are subjected to different hemodynamic forces. Measurements of shear stresses that treat the endothelial surface as flat and ignore the detailed cell topography are found to be less precise than subcellular surface measurements that reveal the spatial heterogeneity of stress distributions.[7] Also, due to their positioning, the ECs are often challenged to react to aggressive factors. They respond to these factors in succession, at first by regulation of their constitutive functions (permeability, rearrangement), followed by EC dysfunction (new functions, impairment), and ultimately cell damage and apoptosis when these become persistent.

ECMs have been also used in *in vitro* experiments (e.g., "organ-on-a chip" and narrow-gap rheometry). The ECM as the product of endothelial tissue culture paved the way for regulated studies of the effects of hemodynamics acting upon ECs and the mechanisms involved.[6,8] Although cell culture models serve as surrogates of tissues and organs for costly animal studies,[9] cultured cells commonly fail to maintain differentiation and expression of tissue-specific functions once they are removed from the living organism. Biomicrofluidics research exploded with the rise of the field of microelectronics[10] and the introduction of polydimethylsiloxane (PDMS). Further advances in microfluidic and tissue engineering technology led to the introduction of the term organ-on-a-chip.[11]

Additionally, ECMs have been adopted for studying the mean rheological properties of individual ECs since they can provide more reliable statistical measurements. This application of the ECMs is also the motivation of the present study due to their superiority and robustness in comparison to single EC techniques. Recent studies (e.g., Ref. 12) have focused on the discrepancies in measuring cell mechanical properties. In the case of single EC techniques, Wu *et al.*[12] noticed that there is a large variation in the average values of the measured moduli among the tested methods and concluded that the results depend highly on the specificities of the method itself. Indicatively for the Atomic Force Microscopy (AFM) method, there was more than

a tenfold difference in the mechanical properties that depended on the measuring parameters and the probed region of cells, a finding that underlines the importance of selecting a measuring technique attentively. In single-cell rheometry, the sample needs to be reduced to the order of micrometers since that is the scale of a cell. To alleviate these limitations, Fernández *et al.*[13] introduced a narrow-gap rheometer that allowed the studying of the cell rheology under oscillatory shear and came to the conclusion that a comprehensive study of cell mechanics cannot be performed by probing only the linear viscoelastic moduli, but it is required to explore ways to induce nonlinear responses. Dhakil *et al.*[14] managed to reach the linear viscoelastic range at small deformations and quantify average mechanical cell properties by introducing a narrow-gap device that functioned in unidirectional shear. Narrow-gap rheometers are advantageous in that they allow the placing of the cells just a few hours before the experiment, live evaluation of cell strain during deformation as well as normal stresses quantification, gap width adjustment, elongation, and compression of the cells, and high reproducibility.[15]

From a mechanical perspective, the ECMs exhibit significant variations when they are subject to a flow field. The variations depend on the flow type, the flow orientation, and the magnitude of the flow field.[16–19] The response of ECMs to prolonged steady flow (maximum shear stress of 34 dynes/cm^2) has been studied experimentally by Eskin *et al.*[16] They provided data for alterations in cell morphology, confluence, and orientation. They also showed that although the cell form changed in response to shear stress, the cell area was not influenced by exposure to flow. Kataoka *et al.*[17] examined the effect of flow direction on the cultured ECs morphology. Experiments on shear flow exposure (2 Pa) were performed for one-way, reciprocating, and alternating orthogonal flows using a parallel plate apparatus. Measuring the shape index and angle of cell orientation, they found that endothelial cells under the one-way flow condition demonstrated substantial elongation and aligned with the flow direction, while in the case of the reciprocating and the alternating orthogonal flows, cells did not elongate as strongly. They reached the conclusion that ECs can be expected to recognize the flow direction and alter their shape and F-actin structure. Similar conclusions were drawn by Levesque and Nerem.[18] Dewey *et al.*[8] employed a cone-plate device that developed uniform fluid shear stress on cultured ECMs. They showed that when exposed to a laminar shear stress of 5–10 dynes/cm^2, confluent monolayers progressively alter their cell form from a polygonal to an ellipsoidal shape and orient with the flow. Also, they suggested that there is a direct correlation between imposed fluid mechanical forces and both endothelial cell structure and function. Dieterich *et al.*[19] designed a more sophisticated apparatus allowing the entire processing control and image data analysis for estimating transient cell motility, alignment, and elongation. They discovered that endothelial cells within confluent monolayers displayed a characteristic phase behavior depending on the applied shear stress, which followed a specific time course: resting (phase I), motility change (phase II), beginning of alignment (phase III), and cell elongation (phase IV).

The goal of the present work is to propose a fluid–structure interaction (FSI) model for studying phase I of ECMs in small-gap rheometers. The model incorporates a periodic layer of ECs (monolayer). It accounts for the membrane, the nucleus, and the cytoplasm and also considers the dual nature of their cytoplasm by taking into account the co-existence of a fluid cytosol that flows around the hyperelastic filamentous network of the cytoskeleton (CSK). Hence, we assume that both the quantification of the developing stresses inside the cytoplasm and the nucleus and the investigation of the deformation of the cell due to the shearing of plasma will be closer to true values. Also, we simulate the complex flow patterns developed around an EC and the intercellular space. This problem retains the main difficulties associated with the solid–porous media coupling. So far, there are only a few rigorous contributions to this type of problem in the field of numerical modeling. Zakerzadeh *et al.* resorted to a loosely coupled splitting scheme designing a time-advancing scheme that facilitates the independent solving of the governing equations of the system at each time step. The main drawback of such loosely coupled splitting schemes is the possible lack of stability and accuracy.[20] Using the mathematical homogenization theory, "Reference Volume Averaging," which has been extensively applied in engineering science,[21–24] we consider a continuous description of the porous medium, where fluid and solid are modeled as overlapping continua and, therefore, the actual interface is not solved explicitly.[25] Implementing this methodology, the porous medium can be modeled without the need for detailed knowledge of the pore geometry.

Primary theoretical works treated a cell as a "sac" of Newtonian fluid that adopts the shape of its membrane, without taking into consideration the elastic nature of the cytoplasm.[26,27] Several subsequent works describe the cell as a purely elastic solid, ignoring hydrodynamic effects. More realistic models present the cytoplasm as a medium that exhibits both viscous, elastic, and plastic behaviors, whose dynamics are described in terms of viscoelasticity, viscoplasticity, or even elastoviscoplasticity.[28,29] These formulations are based on the assumption of a single homogeneous phase while ignoring the microstructure of the cytoplasm, which consists of ions, large aggregates of proteins, and organelles.[30] The assumption of no relative motion between the involved phases that viscoelastic, viscoplastic, and elastoviscoplastic (EVP) notions implicitly entail is flawed. The presence of the polymer network affects the rheological properties of the mixture. Modeling the fluid mechanics of this process requires a description beyond a single velocity field and single stress tensor. One other limitation of single-phase continuum descriptions is that the composition of the material may be dynamic. For example, there can be an exchange of material between the solid and liquid states as in the polymerization/depolymerization of actin network in the cytoplasm (change in solid/fluid volume fraction).[31] Among others, poroelasticity is a formalism that accounts for the dynamics inside the cytoplasm and includes the relative movement between the fluid and solid components of the cytoplasm,[32] since it predicts the movement of liquid through a soft, porous mesh.[33–38] The poroelastic model can also be used to describe diverse cellular phenomena happening at sufficiently short time scales, smaller than the characteristic time at which the cytoskeleton exhibits fluid behavior. The resulting equations describe the cytoskeleton as a hyperelastic solid coupled to a fluid in contrast to earlier works that model the cytoskeleton itself as an active fluid,[39] which was derived to account for cellular processes at long time scales, where fluidization of the cytoskeleton can occur.[40]

II. MODELING

A. Problem formulation

We construct a two-dimensional (2D) arrangement similar to Couette flow, representing the blood plasma (in short, plasma) flow

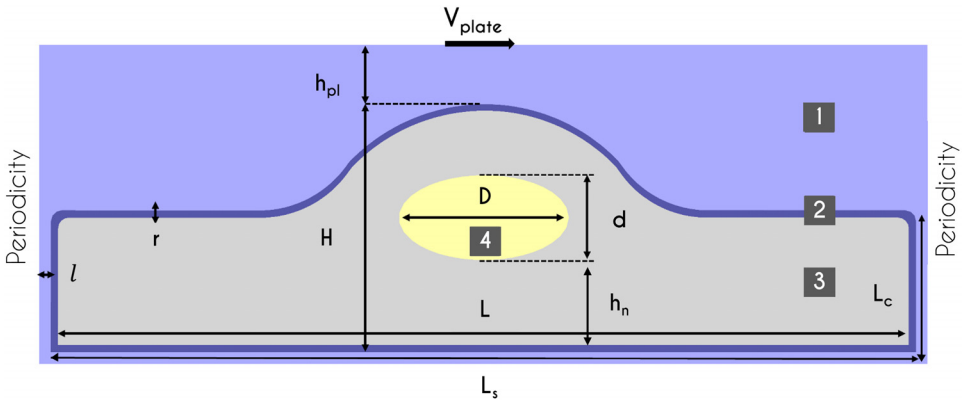

FIG. 1. Control volume and geometric characteristics of the subdomains: the plasma region (1), the cell membrane (2), the cytoplasm (3), and the cell nucleus (4).

field in shear rheometers or the annular section of microchannels lined with ECs. The upper boundary (plate) is assumed to move with a constant velocity to study the shearing effect on ECs, while the conditions on the left and right boundaries are periodic to simulate an infinitely long monolayer. The subdomains that constitute the physical domain include a fluid phase that corresponds to the plasma [(1) in Fig. 1], a thin solid domain that represents the cell membrane [(2) in Fig. 1], a biphasic domain that embodies the cell cytoplasm [(3) in Fig. 1], and an elliptical elastic domain that represents the cell nucleus [(4) in Fig. 1]. The contact of elastic subdomains (membrane, cytoskeleton, nucleus) with the plasma and the cytosol material gives rise to fluid–structure interaction (FSI) phenomena, between plasma and cell membrane, as well as biphasic-structure interaction (BSI) phenomena, between the poroelastic cytoplasm, cell membrane, and nucleus.

The shape and size of the ECs vary across the vascular tree, but they are generally thin and slightly elongated, with their dimensions being roughly 50–70 μm long, 10–30 μm wide, and 0.1–10 μm thick. They are oriented along the axis of the vessel, minimizing the shear stress exerted by the flowing blood plasma.[5] The nucleus at the center of each EC is located ~1.3 μm above the cell base, and it has an oblate ellipsoid shape with a major axis of 8 μm length and a minor axis of 4 μm length.[41] The overall plasma membrane width ranges between 4 and 10 nm.[42] The plasma layer has a thickness of the order of 1 μm.[43] The formed clefts between neighboring ECs are large aqueous pores of width 0.1–0.2 μm.[44] Scanning electron micrographs of spleens demonstrated that in many areas, there were numerous oval gaps or apertures between the lining ECs, with their diameter varying from 0.5 to 4 μm.[45] In the present paper, the values of the geometric characteristics, defined in Fig. 1, are given in Table I; the nucleus is assumed to be an ellipsoid located at the center of each EC and 3.54 μm above the cell base.

At this point is necessary to point out basic limitation of the model. By reducing the problem into two dimensions, we are not able to predict alignment in the third direction, which might be important due to the asymmetric configuration of ECs. Moreover, the prediction of the peripheral interaction with neighbor cells is limited, while the glycocalyx layer is not considered in the present form of the model.

B. Material properties

The material properties used in our simulations are summarized in Table II. Plasma is treated as a Newtonian fluid. The cell membrane and nucleus are modeled as hyperelastic solids following the Saint Venant–Kirchhoff model. On the other hand, the choice of cytoplasm and mechanical properties is rather challenging. Given that the cytoplasm consists of cytosol (e.g., water, ions, metabolites, soluble proteins) and cytoskeleton (CSK) (e.g., aggregates of proteins, as well as organelles), it cannot be formulated as a material of one single and homogeneous phase while ignoring the microscopic structure of these individual cytoplasmic entities. From a mechanical perspective, it behaves as either a solid or fluid, depending on the timescale of consideration and the applied load.[37,38] Also, water migrates over the cytoskeleton network. Therefore, to allow for the distinct phases of the cytoplasm, we assume that it is a poroelastic material.

TABLE I. Geometric characteristics of the model features.

Geometric characteristics			References
Cell length	L	40 μm	5
Cell height	H	10 μm	5
Minimum plasma thickness	h_{pl}	2.5 μm	43
Cell membrane thickness	r	0.1 μm	42
Length of nucleus major axis	D	8 μm	41
Length of nucleus minor axis	d	4 μm	41
Nucleus distance from the cell base	h_n	3.54 μm	
Cleft half width	l	0.25 μm	44 and 45
Bottom channel length	L_s	40.5 μm	
Cleft length	L_c	6.0 μm	

TABLE II. Material properties.

Properties			References
ρ_f (kg/m^3)	Plasma density	1000	
η_f (Pa s)	Plasma viscosity	10^{-3}	
ρ_s (kg/m^3)	Solid density	1410	46
E_m (kPa)	Membrane Young modulus	10	49 and 50
E_s (kPa)	Nucleus Young modulus	2.5	48
E_{ps} (kPa)	Cytoskeleton Young modulus	10	47
φ_s	Solid network volume fraction	0.05–0.99	
ν_s	Solid and poro-solid Poisson ratio	0.499	

Given that the backbone molecules of the cytoskeleton are proteins of high molecular weight, such as F-actin, we assume that cytoskeleton density is $\rho_s = 1410\,\mathrm{kg/m^3}$.[46] Research on the mechanical properties of ECs entities is quite limited; however, there have been reports that indicate that the cytoskeleton Young modulus, which mainly consists of F-actin filaments, is of the order of 10 kPa.[47] The cytoskeleton is the major mechanical component of a cell and plays a key role in determining the overall stiffness of cells. The apparent elasticity of the cytoplasm is dependent on both the cytoskeleton Young modulus and the volume fraction φ_s of the solid network. The nucleus Young modulus is set at ~2.5 kPa as proposed by Caille *et al.*,[48] while previous estimates of cell membrane stiffness range from $E_m = 9$ to 4500 kPa (Ref. 49) depending on the inclusion (or not) of the cortex as well.

C. Governing equations

We consider the control volume shown in Fig. 1. For simplicity reasons, the blood plasma flowing above the cell membrane is treated as a Newtonian fluid, so its viscoelastic effects are neglected.[51,52] The fluid (region 1 in Fig. 1) and solid (regions 2 and 4 in Fig. 1) phases, as well as the poro-fluid and poro-solid (region 3 in Fig. 1) will be denoted with the subscripts f, s, pf, and ps, respectively.

The blood plasma dynamics are represented by the momentum balance as well as the continuity equation as follows:

$$\rho_f\left(\frac{\partial \underline{u}_f}{\partial t} + (\underline{u}_f - \underline{w}_f)\cdot\nabla\underline{u}_f\right) = \underline{\nabla}\cdot\underline{\underline{\sigma}}_f, \tag{1}$$

$$\underline{\nabla}\cdot\underline{u}_f = 0, \tag{2}$$

where ρ_f and $\underline{u}_f$ are the plasma density and its velocity vector, respectively. The stress tensor is described via the Newtonian constitutive law,[43,53,54] as

$$\underline{\underline{\sigma}}_f = -p_f\underline{\underline{I}} + \eta_f\left(\underline{\nabla u}_f + \underline{\nabla u}_f^T\right), \tag{3}$$

where p_f and η_f are blood plasma pressure and the dynamic viscosity, respectively.

Equation (1) is expressed in the Arbitrary Lagrangian–Eulerian (ALE) formulation, where the fluid domain is moving, requiring the introduction of the auxiliary (or mesh) velocity $\underline{w}_f$ in the convective term arising from the ALE description, and it is related to the numerical scheme for the solution of the system. The mesh velocity is associated with the displacement vector of the mesh nodes through the following relation:

$$\frac{\partial \underline{d}_f}{\partial t} = \underline{w}_f, \tag{4}$$

with $\underline{d}_f$ representing the displacement vector subjected to the following artificial constraint:

$$\underline{\nabla}^2\underline{d}_f = 0. \tag{5}$$

Similarly, the structural dynamics of the solid regions, which are the hyperelastic cell membrane and nucleus, are governed by the momentum balance [Eq. (6)] and the incompressibility equation [Eq. (7)],

$$\rho_s\frac{\partial \underline{u}_s}{\partial t} = \underline{\nabla}\cdot\underline{\underline{\Pi}}_s, \tag{6}$$

$$p_s = \lambda_s\, tr\underline{\underline{G}}_s, \tag{7}$$

where ρ_s, $\underline{u}_s$, and p_s are the density, local velocity, and pressure of the individual solid domains (membrane, nucleus) and λ_s is a penalty parameter, which coincides with the respective Lamé parameter. Solid kinematics follow the Lagrangian framework, and thus, $\underline{u}_s$ is linked to the mesh displacement vector $\underline{d}_s$ and mesh velocity vector $\underline{w}_s$ via the following relations:

$$\frac{\partial \underline{d}_s}{\partial t} = \underline{u}_s, \tag{8}$$

$$\underline{w}_s = \underline{u}_s. \tag{9}$$

The solid domains (membrane, nucleus) of this study are both considered to follow the Saint Venant–Kirchhoff constitutive model, which is expressed via the second Piola–Kirchhoff stress tensor as

$$\underline{\underline{S}}_s = p_s\underline{\underline{I}} + 2\mu_s\underline{\underline{G}}_s, \tag{10}$$

where λ_s and μ_s are the Lamé parameters, two material-dependent quantities that arise in strain–stress relationships, and are related to solid properties of elasticity and incompressibility through the expressions $\mu_s = \frac{E_s}{2(1+\nu_s)}$ and $\lambda_s = \frac{\nu_s E_s}{(1+\nu_s)(1-2\nu_s)}$, where E_s and ν_s are the Young modulus and the Poisson ratio of each solid domain, respectively. $\underline{\underline{G}}_s = \frac{1}{2}\left(\underline{\underline{F}}_s{}^T\cdot\underline{\underline{F}}_s - \underline{\underline{I}}\right)$ is the Green strain tensor and $\underline{\underline{F}}_s = \underline{\underline{I}} + \underline{\nabla d}_s$ is the deformation gradient tensor. In addition, the second Piola–Kirchhoff stress tensor, $\underline{\underline{S}}_s$, is related to the first Piola–Kirchhoff stress tensor via the expression $\underline{\underline{\Pi}}_s = \underline{\underline{F}}_s\cdot\underline{\underline{S}}_s$.

The Cauchy stress tensor is then defined as

$$\underline{\underline{\sigma}}_s = \left(det\left(\underline{\underline{F}}_s\right)\right)^{-1}\underline{\underline{F}}_s\cdot\underline{\underline{\Pi}}s^T. \tag{11}$$

The governing equations of cytoplasm are more complex since they incorporate the mechanical properties and dynamics of two discrete phases: an elastic solid corresponding to the cytoskeleton and a Newtonian fluid being the cytosol. The two phases are intertwined with each other and are moving at different velocities, leading to relative movement and drag effects between the two phases. The poro-fluid dynamics are governed by the momentum equation [Eq. (12)].[55] The characteristic scales inside the cytoplasm lead to extremely low Reynolds numbers of the order $\sim 10^{-2}$. Even in bigger cells or faster flows, the Reynolds number is much smaller than unity.[56] Therefore, inertia in the cytoplasmic domain can be safely neglected, and Darcy flow constitutes a satisfactory approximation,[57]

$$\underline{0} = -\underline{\nabla}p_{pf} + \xi(\underline{w}_{ps} - \underline{u}_{pf}), \tag{12}$$

where $\underline{u}_{pf}$ is the cytosol density and its velocity vector and $\underline{w}_{ps}$ is the poro-solid mesh velocity, which is defined as $\frac{\partial \underline{d}_{ps}}{\partial t}$. The stress tensor is described via the Newtonian constitutive law as in Eq. (3) with p_{pf} being the cytosol pressure, which is associated with the pressure of the poroelastic mixture p through $p_{pf} = (1-\varphi_s)\,p$ and $\xi = \frac{\mu_{pf}}{\kappa}$ and κ being translated as Darcy's permeability. Some typical values of ξ are in the range between 10 and 50 $\mathrm{pN\,s/\mu m^4}$.[58]

We also define the momentum equation of the poroelastic mixture (consisting of fluid and solid), which is solved in the same domain on a macroscopic scale [Eq. (13)]. Basically, the average microscopic state in the poroelastic domain is represented. It is a simple expedient to achieve a correct coupling between the poroelastic and the hyperelastic domains[59,60]

$$0 = \underline{\nabla} \cdot \underline{\underline{\sigma}}_p. \tag{13}$$

The constitutive equation of the poroelastic mixture is based on the Saint Venant–Kirchhoff, and the model found in Ref. 60 is

$$\underline{\underline{\sigma}}_p = p_{ps}\underline{\underline{I}} + 2\mu_{ps}\underline{\underline{G}}_{ps} + p_{pf}\underline{\underline{I}}, \tag{14}$$

where $\underline{\underline{G}}_{ps} = \frac{1}{2}(\underline{\underline{F}}_{ps}{}^T \cdot \underline{\underline{F}}_{ps} - \underline{\underline{I}})$ is the Green strain tensor and $\underline{\underline{F}}_{ps} = \underline{\underline{I}} + \underline{\nabla} d_{ps}$ is the deformation gradient tensor, μ_{ps}, λ_{ps} are the respective Lamé constants, and p_{ps} is the cytoskeleton contribution to pressure of the poroelastic mixture $p_{ps} = \varphi_s p$. The pressure of the poroelastic mixture (p) subject to the incompressibility constraint of the system [Eq. (15)] is

$$\underline{\nabla} \cdot \left((1-\varphi_s)\underline{u}_{pf} + \varphi_s \underline{u}_{ps}\right) = 0. \tag{15}$$

In the limit of low Darcy's permeability, the first of the terms in Eq. (16) contributes slightly and pressure p_{ps} (and consequently p) can be calculated by

$$p_{ps} = \lambda_{ps}\, tr\underline{\underline{G}}_{ps}. \tag{16}$$

D. Boundary conditions

The fluid–structure interaction (FSI) between the fluid regions and the solid domains comes with the imposition of several conditions on their interfacial boundary. Here, we set a balance between forces from the two sides [Eq. (17)], equality between the corresponding velocities [Eq. (18)], finally, equality between the corresponding local auxiliary (mesh) velocities [Eq. (19)]

$$\underline{\underline{\sigma}}_s \cdot \underline{n}_s = \underline{\underline{\sigma}}_f \cdot \underline{n}_f, \tag{17}$$

$$\underline{u}_s = \underline{u}_f, \tag{18}$$

$$\underline{w}_s = \underline{w}_f. \tag{19}$$

FSI problems when dealing with the coupling of solely fluid and solid domains are somewhat easily manageable since, at the interface of those different phases, we have a force equilibrium meaning that the fluid stresses acting upon the interface are equal to the solid stresses acting on the opposite normal direction at the interface. However, in BSI problems, two distinct interactions and, therefore, couplings have to be formulated. The first one is associated with the interaction between the poro-solid (CSK) and poro-fluid (cytosol) that occupy the same domain in the physical configuration. This interaction is achieved via the imposition of the friction term introduced in the bulk equation of the mixture [Eq. (12)]. The second coupling refers to the formulation of the interaction between the biphasic material (cytoplasm) and the hyperelastic membrane/nucleus. This interaction is modeled by the implementation of the force balance at the interface. This force balance includes the total force of the biphasic cytoplasm (contribution of both poro-fluid and poro-solid) and the exerted force from the hyperelastic membrane/nucleus [Eq. (17)].

On the moving plate region interface of the Couette flow analogous (top boundary in Fig. 1), the velocity is assumed to be constant (V_{plate}) in the x-direction [Eq. (20)],

$$\underline{u}_f = V_{plate}\,\underline{e}_x. \tag{20}$$

On the base of the immobile endothelial cells (bottom boundary in Fig. 1), we impose the no-slip and no-penetration conditions for the velocity.

Regarding the auxiliary velocity, on the top boundary, as well as on the bottom of the endothelial cell, the mesh remains fixed:

$$\underline{w}_f = \underline{0}. \tag{21}$$

The left and right boundaries (Fig. 1) are periodic since we study an infinitely long monolayer.

E. Numerical method

The governing equations are spatially discretized using the finite element method (FEM). In Fig. 2, we can see the tessellation of the blood plasma domain [Fig. 2(a)], the cytoplasmic domain [Fig. 2(b)], the wall and nucleus [Fig. 2(c)]) that were created using the SALOME CAE package.[61] Finally, the discretized domain of the 3D cell is depicted in Fig. 2(d). For the solution of the fluid–structure interaction problem, we implement the full monolithic coupling methodology with the global unknown vector being $X = \{\underline{u}, p_f, p_s, \underline{w}\}$. Poro-solid and poro-fluid pressures, p_{ps} and p_{pf}, are also incorporated in the p_s and p_f unknowns, respectively. The corresponding mixed element is the P2–P0–P0–P2 element. The utilization of the P0 element is necessary to resolve the pressure discontinuity between the two phases. The definition of two "pressures" is critical for the correct coupling of the poroelastic equations and the stabilization of the numerical scheme. The domains are tessellated in triangular or tetrahedral meshes of elements, respectively. Finally, for the time integration, we use the implicit Euler method with the time step of $\delta t = 20\,\mu$s (Table III).

F. Numerical scheme validation and parametrization of the nucleus model

To validate the model and the numerical scheme, we implemented a benchmark test proposed by Caille *et al.*[48] To this end, we consider a spherical domain (Fig. 3) corresponding to either the EC, with an initial radius is $R_o = 10\,\mu$m, as Caille *et al.*,[48] or sole nuclei, with $R_o = 5\,\mu$m, for each test case.

The assumptions of this test are as follows: (a) the cell or its nucleus is spherical before loading, (b) there is plane symmetry, and (c) the contact area also expands laterally upon compression and at a certain force the radius exceeds the initial sphere radius.

Either a cell or its nucleus is introduced between two microplates, the upper one of which is moving downwards with a specific velocity (Fig. 3). During the compression, the force acting upon the sphere is being calculated as a function of the deformation:

Specifically, we quantify the force acting upon the compressed sphere by integrating the normal part of the stress in the appropriate domain[62]

$$\underline{F} = \int \left(\underline{n} \cdot \underline{\underline{\sigma}}_s\right) dS, \tag{22}$$

where S corresponds to the top flattened part of the sphere, $\underline{\underline{\sigma}}_s$ is the total stress tensor either corresponding to the EC membrane or the nucleus, and $\underline{n}$ the outer normal unit vector.

In Fig. 4(a), we observe a very good agreement between our results and those of the experiments in Caille *et al.*,[48] for the compression of hyperelastic nuclei, with a small deviation in the case of $E_{\text{nucleus}} = 10$ kPa at higher deformations.

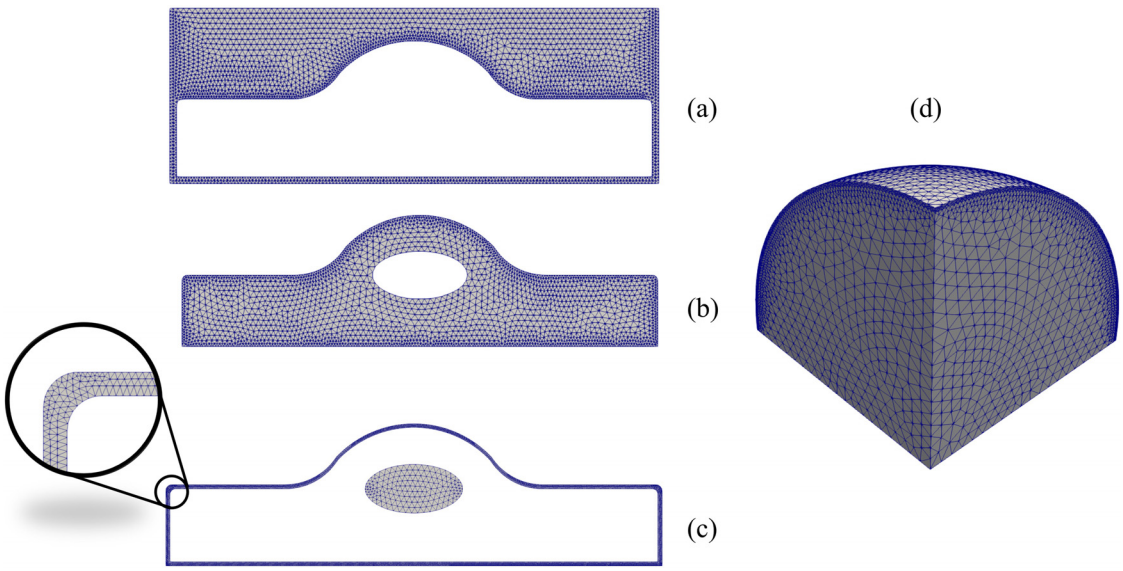

FIG. 2. Tessellated domains of the shear problem and the compression test, respectively. Tessellated domain of (a) the blood plasma region, (b) the cytoplasmic region, (c) cell wall and nuclear domain, and (d) 3D cell for compression test.

TABLE III. Mesh characteristics.

Problem	Min./Max. element size (μm)	Min./Max. element size in cell wall domain (μm)	Total no. elements	Total no. unknowns
2D Shear	$3 \times 10^{-3} / 2.2 \times 10^{-2}$	$3 \times 10^{-3} / 5.16 \times 10^{-3}$	13 556	189 784
3D Compression	$4 \times 10^{-3} / 8 \times 10^{-2}$	$4 \times 10^{-3} / 8 \times 10^{-3}$	68 014	1 496 308

G. Selection of the cytoplasm young modulus

The most challenging part in implementing a poroelastic model to describe the cytoplasm rheological behavior was the selection of the appropriate Young modulus, in that the elastic part of the cytoplasm was now a mere network creating pores in which the viscous cytosol was flowing. In that sense, the elasticity of the poroelastic cytoplasm, which is characterized via a small solid volume fraction φ_s, cannot be equal to that of a robust hyperelastic compound. Thus, we proceeded in retrieving the equivalent elasticity by comparing force-deformation curves with those of the work of Caille *et al.*[48]

To get the same curve as that of both the experimental data presented in Caille *et al.*[48] and their simulation, we need to raise the poroelastic cytoplasm elasticity to $E_{cytoplasm} = 2.2$ kPa for a $\varphi_s = 0.9$, as opposed to their hyperelastic cytoplasm, which has an elasticity equal to 1.0 kPa. This value of course depends on the chosen solid volume fraction. The smaller the cytoskeleton volume fraction, the larger the cytoplasm Young modulus. Hence, for a volume fraction ranging from 0.001 to 0.999, the corresponding elasticity varies from 2.2 MPa to 2.2 kPa. The upper bound of φ_s is an extreme value that we use it in order to demonstrate the predictability of the model. In Fig. 5, we observe that the solid volume fraction affects the elasticity of the

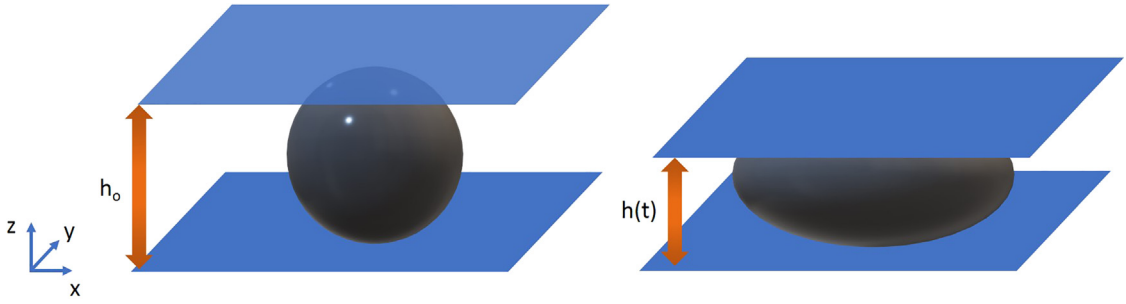

FIG. 3. Compression test, where h_o is the initial distance of the parallel plates and also height of the spherical cell and h is the instantaneous distance of the parallel plates.

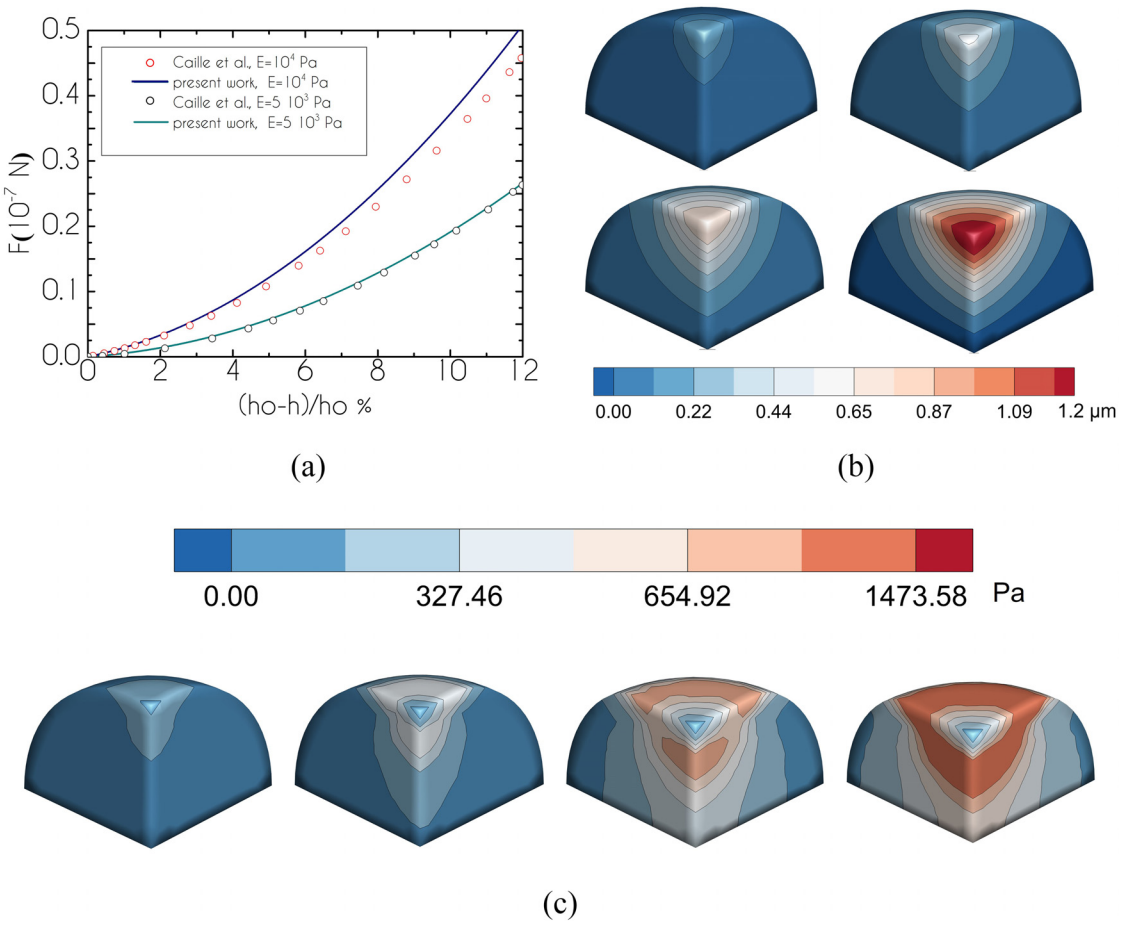

FIG. 4. (a) Force-deformation curves of nuclei compression. h_o is the initial height of the spherical cell and h is the current height during compression. Circles depict the Caille *et al.*[48] results, and lines correspond to our analysis results. (b) Nuclei displacement field contours. (c) Second invariant of Cauchy stress tensor in Pa for the nucleus compression case of E = 10 kPa.

poroelastic cell, yielding distinct force deformation curves. Since the volume fraction of the solid cytoskeleton varies in every cell, this graph is an indicator of how much force is needed to compress various cells. A force in the range of 0.1 to 0.65 $\times$ 10^{-7} N is required to achieve the same deformation.

III. RESULTS AND DISCUSSION

A. Base case analysis

As a base state, we apply a constant velocity of $V_{plate} = 5.5$ mm/s, given in Table IV, along with the other relevant parameters. Even though with this choice, which represents a normal flow (e.g., through a microvessel), we cannot observe acute deformations and reshaping of the ECs, and it provides information about the dynamics of the interacting plasma-EC system such as the developing stresses, the effect of Wall Shear Stress (WSS), recirculation zones, and the condition of flow through the clefts between successive cells. The rest geometric characteristics are summarized in Table I.

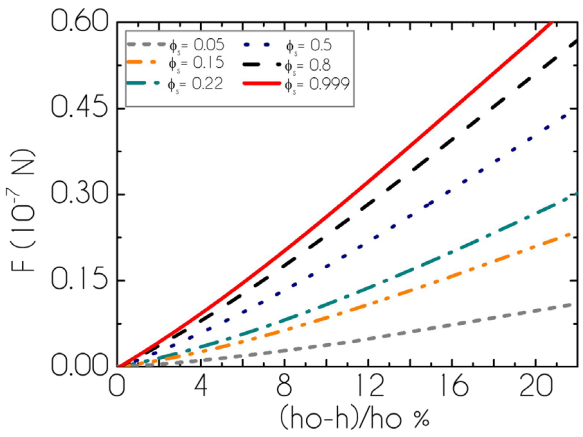

FIG. 5. Force vs deformation curves for cells with various volume fractions φ_s of the cytoskeleton, under compression for a fixed Young modulus of cytoskeleton $E_{cytoplasm} = 10$ kPa.[48]

TABLE IV. Base state case.

Base state		
Plate velocity	V_{plate}	5.5 mm/s
Cytoskeleton volume fraction	φ_s	0.22
Minimum plasma layer height	h_{pl}	2.5 μm
Cleft width	l	0.25 μm

After imposing the motion, the velocity, and the corresponding stress fields develop gradually. The fields reach a steady state quite fast. The steady velocity field in the plasma region is portrayed in Fig. 6.

At the upper plate, bounding the plasma, the x-component of the velocity field has been set. Proceeding downwards along the y-axis, the velocity decreases, reaching a zero value at the zone where flow stagnation occurs. In the recirculation zones, u_x has negative values; the flow is in the opposite direction, and the streamlines take the form shown in Fig. 7. Overall, the streamlines follow two different patterns. There is an extended flow recirculation in the lower cavity region between the interface peaks of two neighboring cells and a region where the velocity varies linearly, and the streamlines are almost parallel to the moving plate. There is a stagnation point at the cell interface, close to which the streamlines start to follow opposite directions, causing increased extensional stresses on the cell membrane (point B). The magnitude of the WSS for the base state case is indicated by the different colors in Fig. 7. Its maximum value is located at the top of the cell protrusion with $WSS = 5.1$ Pa. At the stagnation point, around the middle of the protrusion sides, the WSS turns to zero. Proceeding along the lateral horizontal sides of the upper cell, WSS takes negative values, reaching a maximum negative value equal to -0.57 Pa. This variation of WSS values throughout the cell wall (-0.57–5.1 Pa) that stems from the shearing of the imposed flow is considered significant. Thus, an assumption of uniform WSS over the endothelium, as Dabagh *et al.*[63] adopted, would be an oversimplification and would not correspond to actual conditions.

Additionally, our calculations indicate that a very small horizontal displacement of the cell arises, of the order of 10^{-2} μm. The only region which is somewhat exposed to increased shear and would be possible to observe deformations is the protrusion of the cell geometry. In Fig. 8(a), the displacement of the top point is portrayed, until it reaches an asymptotic steady state having the maximum deformation. In that state of the cell maximum deformation, internally developed shear stresses and WSS are also maximum [Fig. 8(b)]. Similar displacement values in the flow direction are retrieved by Dabagh *et al.*,[63] who demonstrate maximum displacement at the cell protrusion of the order of 0.05 μm.

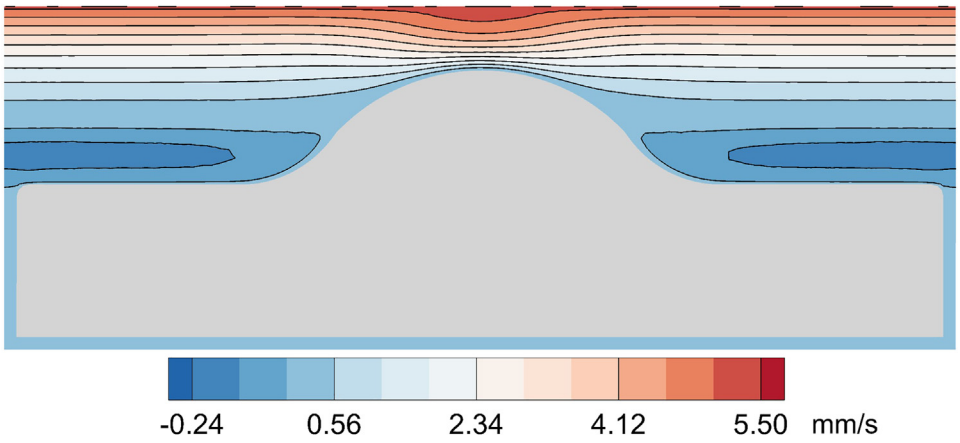

FIG. 6. x-component of plasma velocity at the steady state for the base case.

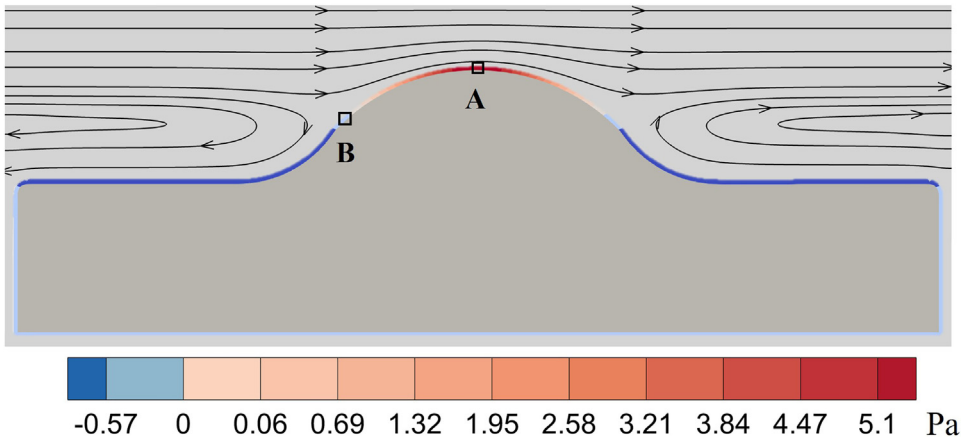

FIG. 7. Streamlines and WSS contour for the base case at steady state. Minimum and Maximum values of WSS are indicated. Two important regions on the cell membrane (A-top point and B-side point) are also depicted.

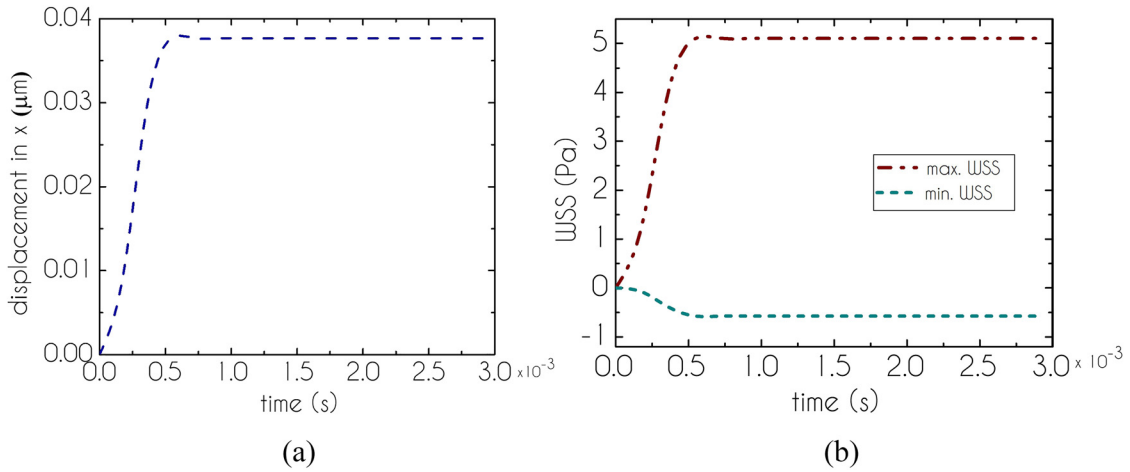

FIG. 8. (a) Displacement in the x-direction of the top point (point A in Fig. 7) of the cell protrusion in time. (b) Minimum and maximum WSS values in time for the base case.

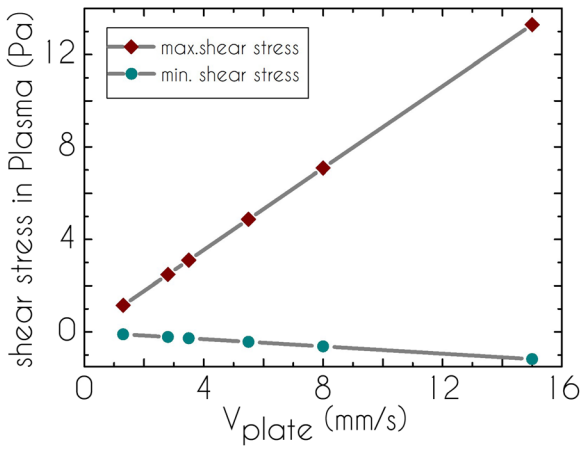

FIG 9. The steady shear stress within the plasma region as a function of the imposed plate velocity V_{plate}.

The stresses inside the cytoplasmic region are owed to the cell deformations that are caused by the shearing of the plasma flow. This shearing results in the deformation of the ECM. Due to the elastic stiffness of the ECM, even slight deformations lead to impactful stresses. Our analysis permits the investigation and calculation of internal stress inside the structure of the body.

B. Effect of the imposed top plate velocity, V_{plate}

We proceeded by examining the effect of different values of V_{plate} on the ECM under normal and extreme conditions. The EC morphology, metabolism, and structure have been found to vary with the shear strain-rate of the blood.[8] We proceeded with the determination of the stresses over and inside the ECs. The maximum and minimum shear stress values for each velocity are given in Fig. 9. In Fig. 10, the shear stress field inside the plasma region for the extreme plate velocity case ($V_{plate} = 15.0\,\text{mm/s}$) is presented. A plate velocity equal to $V_{plate} = 15.0\,\text{mm/s}$ can be acute for a microchannel of $2.5\,\mu\text{m}$ height in physiological states, but in the case of pathological events, such as

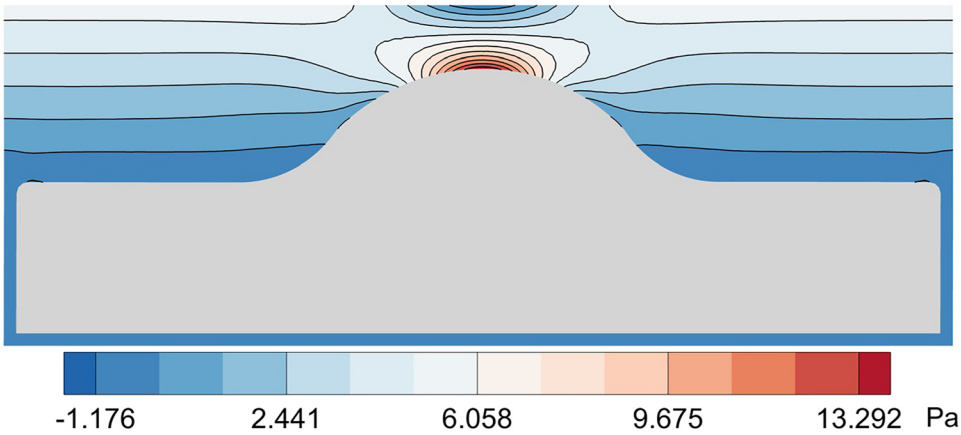

FIG. 10. Steady shear-stress contours in the plasma region for various $V_{plate} = 15.0\,\text{mm/s}$.

TABLE V. Corresponding plate shear rates with varying V_{plate}.

$h_{pl} = 2.5\ \mu$m			
V_{plate} (mm/s)	Plate shear rate (s^{-1})	Comment	References
1.3	520	Physiological in microvessel	64
5.5	2200	Physiological in microvessel	
15.0	6000	Extreme	

tachycardia, hypertension, or atherosclerosis, which leads to the narrowing of the vessel, it can often be encountered. In these cases, it is important to know which are the flowing conditions over the ECM, and which are its effects to it. The shear rates under investigation are summarized in Table V.

As we observe in Fig. 9, there is a linear dependence of both the maximum and minimum shear stress in the plasma region on the imposed top plate velocity. The location of the extreme values can be seen in Fig. 10. This is reasonable since shear stresses in the plasma region are retrieved via the gradient of velocity. Thus, if $u_f = V_{plate}$ is the imposed velocity on the moving plate, and $u_f = 0$ at the cell membrane, then the shear stress will be $\tau_{xy} = \eta_f \frac{\partial u_f}{\partial y} \approx \eta_f \frac{V_{plate}}{h_{pl}}$, demonstrating a linear dependence on V_{plate} and an inverse dependence on h_{pl}. Interestingly, negative values of shear stress are encountered inside the plasma region. We recognize that these values are located mainly at the concave regions of the cell geometry and are developed where the flow has changed direction.

Regarding the WSS variation, the vascular system can be viewed as a self-organized homeostatic system.[65] The physiological average value of WSS is not uniform throughout the arterial network but may vary locally. The WSS values at steady state for various velocities ranging from 1.3 to 15 mm/s are depicted in Fig. 11. Maximum WSS is located at the top of the dome, then turns to zero locally at the height where flow stagnation occurs and subsequently takes negative values at the concave regions of the cell geometry due to the eddy above those regions where opposite flow is encountered. The point at which the flow takes opposite directions, acting upon the wall as a "stretcher," is the point where wall thinning could occur and consequently possible rupture of the wall. We do not expect that minor eddies throughout the intercellular clefts will have the same effect on the cell membrane, but at the primary flow region such as at the concave region between successive cells, where major recirculation zones appear, wall thinning could be significant.

As the imposed plate velocity increases, both the maximum WSS value at the top of the cell protrusion, and the negative WSS values, located at the lateral horizontal sides of the upper cell wall, increase also. The point of zero WSS value is the same for every imposed velocity case and coincides with the point of the flow separation at the middle part of the left and right side of the protrusion. Picking the maximum and minimum values of WSS on the ECM, we seek the relation between them and the imposed shearing velocity. As shown in Fig. 11(b), there is a linear variation of both maximum WSS and minimum WSS with the applied V_{plate}, a case that is in accordance with the Couette flow relation for WSS and flow velocity. The Couette relation suggests that any increase in hemodynamic demand translates into a linear elevation in shear stress, whereas a narrowing in vessel lumen by, for example, pathophysiological events, may lead to an increase in the shearing stress imposed on the ECM, following an inverse function. Therefore, it is interesting to examine the relation between WSS and h_{pl}, which is an indicator of the vessel lumen.

The imposed top plate velocity has its impact on the cytoplasmic shear stresses. In Fig. 12, we see the shear stress contours inside the cytoplasm. The stresses are computed by the shear components of the poroelastic mixture stress tensor, $\underline{\sigma}_p$, which is given by Eq. (14). We recognize a linear relation between shear stress and plate velocity even inside the poroelastic cytoplasm. This is because the deformations of the cell are not big enough under these conditions. Inside the cytoplasm, there are no negative values of shear stress as in the plasma region, hinting that the cell deformation is in the direction of the flow only.

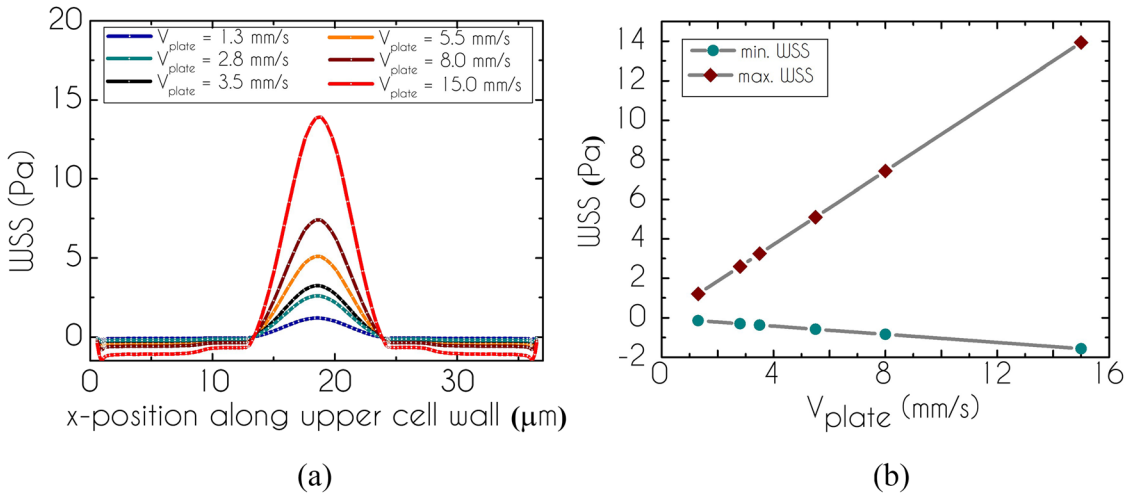

FIG. 11. (a) WSS values vs the x-position on the upper cell wall for various plate velocities, V_{plate}. (b) Minimum and Maximum WSS (on the membrane) values for various plate velocities.

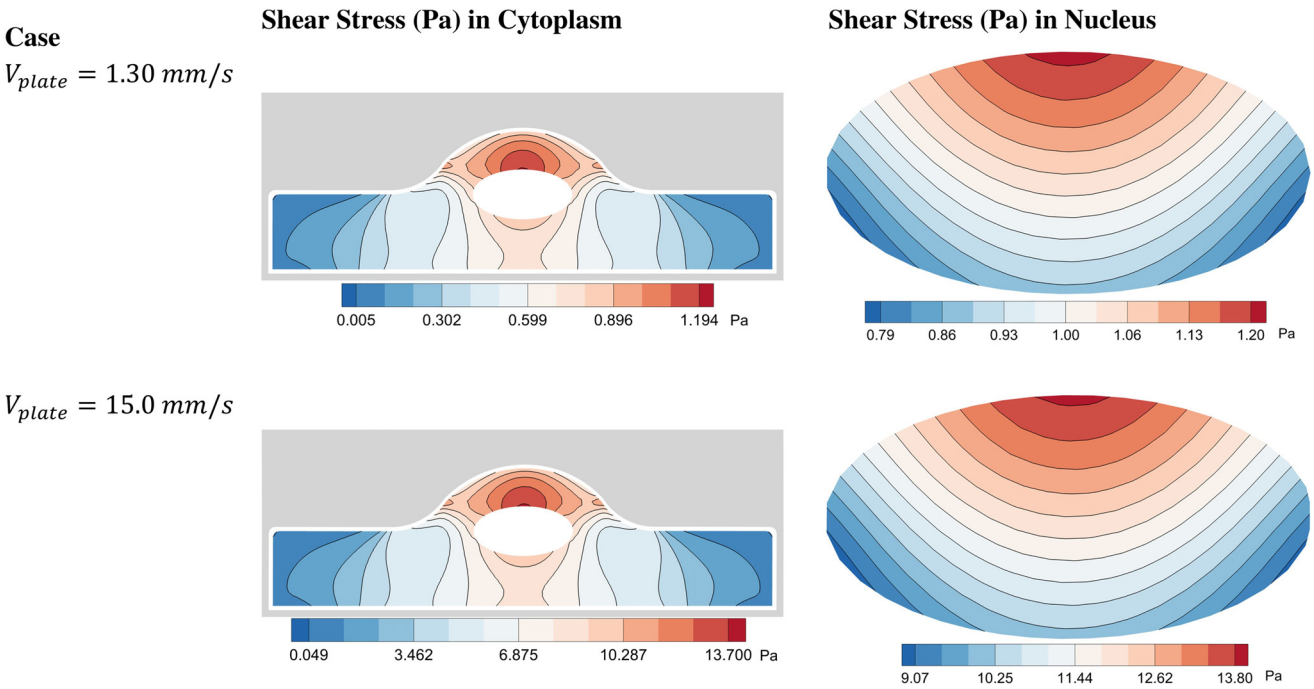

FIG. 12. The steady shear stress contours in the cytoplasmic and nuclear region for various plate velocities. The plots are banded with 13 contour levels.

Shear stresses develop inside the nucleus also (Fig. 12). It is vital to know how the nucleus is affected and hence the gene regulation, under shear.[66] An advantage of our proposed model for the cytoplasm is that we can quantify the shear stresses inside the nucleus. The shear stresses are computed by the corresponding components of the hyperelastic solid stress tensor $\underline{S}_s$, which is given by Eq. (10). As observed in Fig. 12, there are no negative shear stresses inside the nucleus, and the minimum shear values are located mostly at the bottom of the elliptically shaped nucleus. Maximum shear stresses are prominent at the top part of the nucleus.

The stress variation between the distinct velocity cases in Fig. 12 can be observed through the contour level legend. Maximum shear stresses are located mostly at the cell protrusion and around the nucleus and are more prominent in the three last cases of plate velocity where shearing is more intense.

Both minimum and maximum values of shear stress inside the cytoplasmic region display a linear dependence on the imposed top plate velocity. The linear trend of the graphs shown in Fig. 13(a) is justified since the deformation of the cell is not acute under these shearing conditions. The displacement of the cell in the y-direction is not

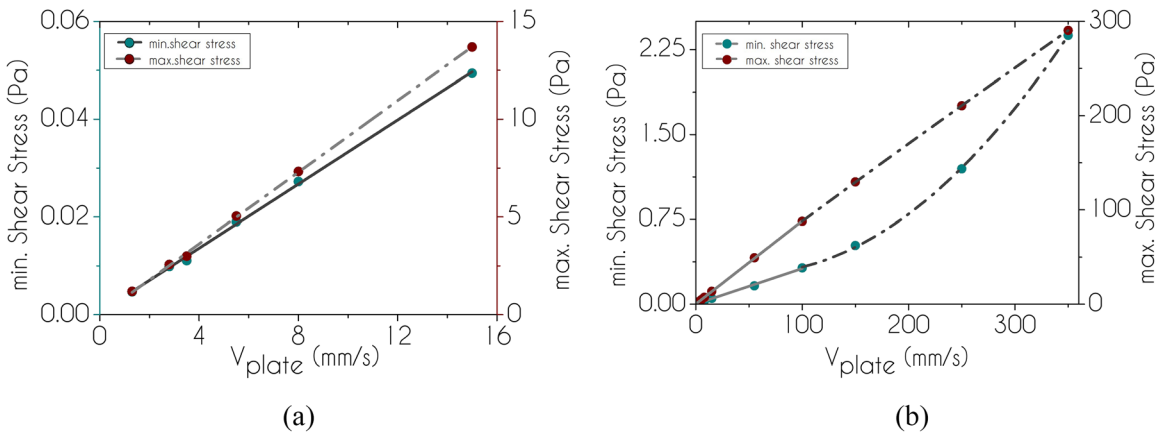

FIG. 13. (a) Minimum and Maximum steady shear-stress values within the poroelastic cytoplasm under physiological plate velocities. (b) Minimum and maximum steady shear stress values inside the poroelastic cytoplasm under extreme plate velocities.

significant, and hence, the linear behavior of shear stress to strain prevails. Case in point, we investigated the shear stress values in the cytoplasm for even higher plate velocities in order to see the behavior of the cell under both normal and extreme conditions. For plate velocities ranging from 1.3 to 350 mm/s, there are two distinct regions in Fig. 13(b) of both minimum and maximum shear stress vs plate velocity that we can recognize; a linear region from 1.3 to 100 mm/s and a quadratic one from 100 to 350 mm/s.

It should be noted at this point that the shear stresses that emerge due to the fluid part of the cytoplasm are very low in comparison to those under these conditions. The effect of the hydrodynamic shearing inside the cytoplasm would be more prominent in the case of extreme deformations, under very high shearing velocities, but they would still be several orders of magnitude lower than those of the solid contribution.

Although the top of the cell protrusion is exposed to higher fluid shear stresses, it does not experience high normal stresses (Fig. 14). These are distributed symmetrically to the cytoplasm region, with positive $\tau_{xx} = \underline{\sigma} : \underline{e}_x\underline{e}_x$ stresses at the left side of the cell and negative τ_{xx} stresses at the right. Therefore, the cell experiences compressive stresses at both sides, with the highest positive (negative) values left (right) from the concave region that forms between the cell protrusion and the horizontal lateral parts of the cell luminal surface. The positive/negative normal stresses increase/decrease with increasing plate velocity but do not exceed in magnitude the shearing of the cell. In fact, the two values, shear stress and normal stress, deviate more than 25%.

Similarly, the τ_{yy} stress inside the cytoplasm assumes negative values at the left side of the cell and positive values at the right [Fig. 14(b)]. This means that the cell feels compressive stresses at the left side and extensional stresses at the right one, as if it is pushed and pulled simultaneously at its two lateral sides.

The normal stresses that develop inside the nucleus are of the same order of magnitude but not as significant as the shear ones. As we see in Figs. 14(c) and 14(d), the maximum absolute value of the stress reaches a peak value of 3 Pa for the maximum imposed velocity $V_{plate} = 15$ mm/s, whereas for the same V_{plate}, the value of the shear stress is equal to almost 14 Pa; thus, the normal stresses are almost 22% of the shear ones. The τ_{xx} stresses are distributed in the same way

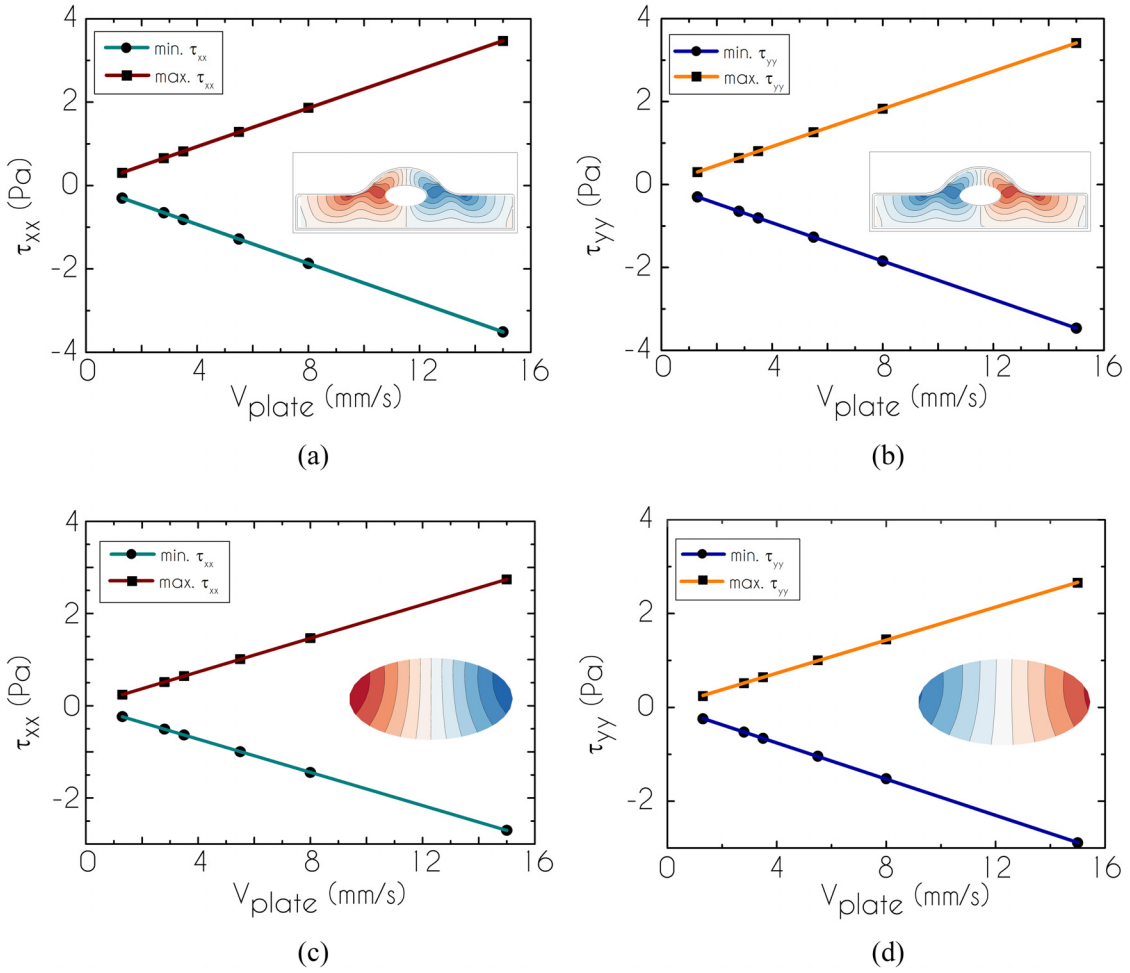

FIG. 14. Normal stresses in the cytoplasm for various plate velocities (a) τ_{xx} and (b) τ_{yy}. Normal (c) τ_{xx} and (d) τ_{yy} stresses inside the nucleus for various plate velocities.

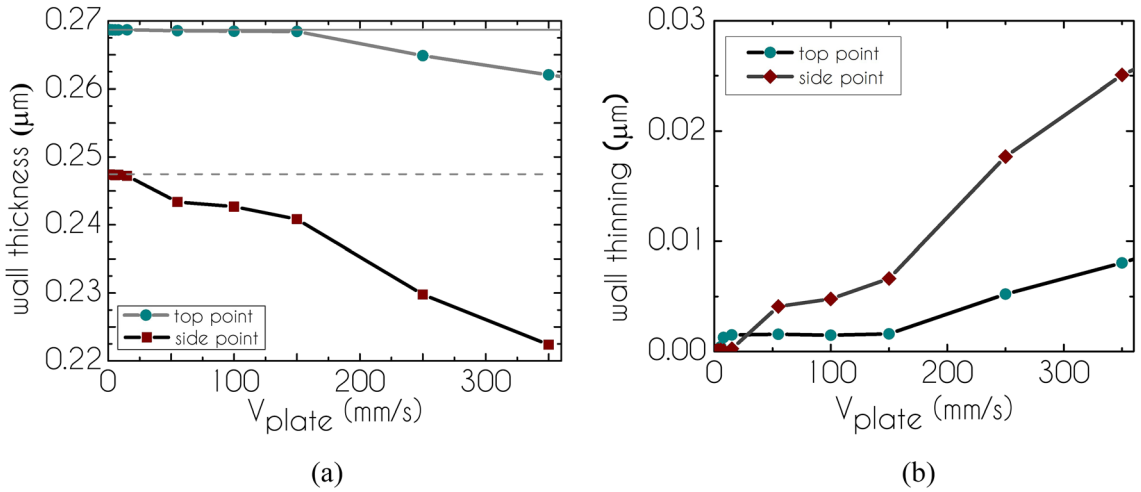

FIG. 15. (a) Wall thickness values at the point of flow stagnation (point B in Fig. 7) and the top point of cell protrusion (point A tin Fig. 7) under various plate velocities. (b) Comparison of wall thinning at the top point of the cell protrusion and at the point of flow separation under various plate velocities. The dashed line corresponds to the initial wall thickness of the side point and the solid line to the initial thickness of the top point.

as in the cytoplasmic region, with positive values at the left side and negative values at the right, indicating a lateral compression of the nucleus as well. The highest τ_{xx} values are located left and right of the elliptically shaped nucleus, hinting that they originate from the lateral sides of the cytoplasm and not from the cell protrusion, since at that region normal stresses are not prevalent. The τ_{yy} stresses demonstrate an opposite distribution inside the nucleus, with positive values at the right and negative at the left, hinting anticlockwise rotation of the elliptical nucleus. A similarity to the development of shear stresses is that normal stresses as well evolve linearly as a function of V_{plate}, both in the cytoplasm and the nucleus.

We proceeded in quantifying the effect of the applied plate velocity on the wall thickness at the point where flow stagnation occurs, in order to examine wall thinning because of it. In Fig. 15(a), we investigated the magnitude of wall thickness for the broader plate velocity range from 1.3 to 350 mm/s. In the graph, we discern two plateaus and two regions of fast reduction of the wall thickness with the applied velocity. The first plateau is for the range of 1.3 to 15 mm/s where there is only a slight change in the wall thickness, of the order of $10^{-4}\,\mu$m. A steep region follows for the range of 15 to 60 mm/s where the thinning is greater. Reaching the second plateau for the range of 60 to 120 mm/s where the wall thickness remains constant. Finally, under extreme velocities, in the range of 120 to 350 mm/s, there is an acute reduction of the wall thickness reaching the value of 0.225 μm. Beyond this velocity range, extreme deformations on the mesh elements cause the numerical solver to fail. This could be associated with the fact that the rigidity of the cell membrane is not able to withstand the magnitude of this specific hydrodynamic load, leading to its rupture (Fig. 16).

It is reported in the literature that high WSS affects the wall thickness and is the region most prone to wall thinning. After quantifying the wall thickness at the top of the cell protrusion (where the highest values of WSS appear) [Fig. 15(a)], we conclude that, in our case, wall thinning is more prevalent at the flow stagnation point rather than at the top of the cell protrusion, although some wall thinning occurs there also. There appears one plateau and two steep linear regions of wall thickness reduction. The magnitude of wall thinning at the two distinct locations of the cell membrane is more obvious in Fig. 15(b). For lower imposed velocities, in the range of 1.3 to 15 mm/s, wall thinning is slightly more prevalent at the top of the cell protrusion. Therefore, we conclude that the extensional forces acting upon the lateral sides of the cell wall due to the flow separation are more significant than the force due to the maximum shearing at the top.

C. Effect of the minimum plasma layer height, h_{pl}

We investigate the effect of h_{pl} on *WSS* for $h_{pl} = 1.6$, 2.5, 5.0, 7.5, and 10.2 μm, ranging from relatively small to large values. The derived relation is comparable to that of a Couette flow. In the Couette case, WSS and vessel's lumen are related as h_{pl}^{-1}, while in our case, the relation derived is $h_{pl}^{-1.012}$ (Fig. 17).

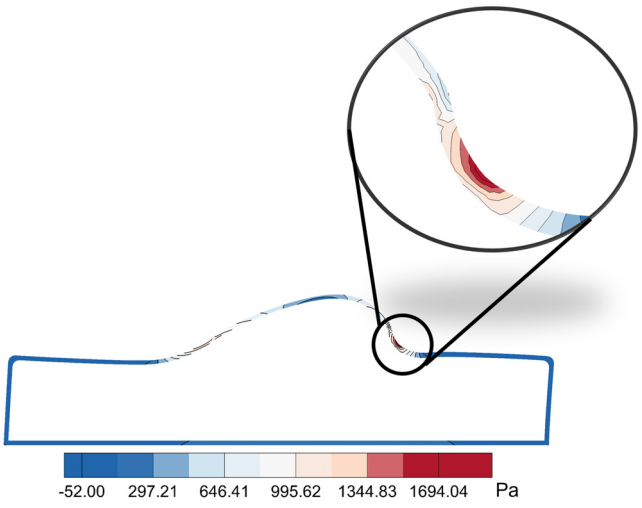

FIG. 16. Case of $V_{plate} = 450$ mm/s. Shear stress distribution in the cell membrane reaching a maximum value of 1868 Pa.

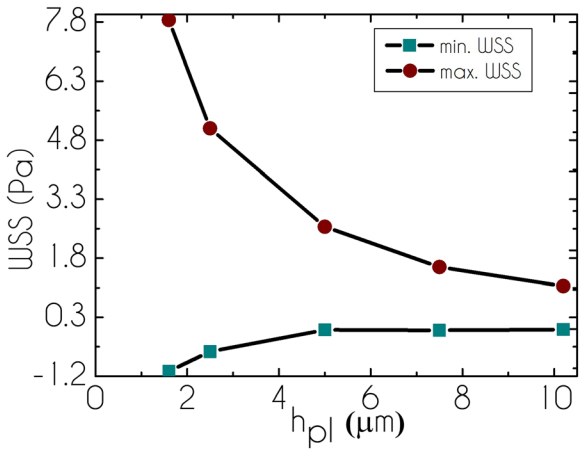

FIG. 17. Maximum and minimum steady WSS values for various h_{pl}.

TABLE VI. Corresponding shear rates to investigated plasma heights, h_{pl}.

$V_{plate} = 5.5$ mm/s			
h_{pl} (μm)	Plate shear rate (s^{-1})	Comment	References
1.6	3437.5	Extreme	64
2.5	2200	Physiological in microvessel	
5.0	1100	Physiological in microvessel	
7.5	733.33	Physiological in microvessel	
10.2	539.215	Physiological in microvessel	

The graph (Fig. 17) of the minimum WSS as a function of h_{pl} suggests that for this range of height values, the minimum WSS abruptly increases and then reaches the asymptotic value of ~ -0.05 Pa.

Regarding the effect of the minimum plasma layer height, h_{pl}, on the wall thinning at the aforementioned range of h_{pl}, we observe that it is not as significant as the effect of the imposed velocity, because for plate velocity of $V_{plate} = 5.5$ mm/s, it does not result in significant shearing rates, as seen in Table VI.

Hence, the variation of the wall thinning occurs at the fourth decimal. It is clear in Fig. 18(c) that for all h_{pl} cases, wall thinning is more prominent at the side point of stagnation flow than at the top point of maximum shear. Wall thickness vs h_{pl} diagrams [Figs. 18(a) and 18(b)] portray an asymptotic trend. Hence, for even higher h_{pl} cases, where the shearing decreases, the deviation of the wall thickness from its initial value is more significant at the point of stagnation, while at the top point of the cell protrusion the wall has almost retained its initial thickness.

IV. CONCLUSIONS

A two-dimensional model was developed for investigating the dynamics of an adherent ECM in a cartesian Couette geometry under startup flow conditions leading to a steady state. ECs feature both FSI and BSI principles, correctly coupling together a poroelastic cytoplasm to membrane and nucleus hyperelastic domains and these to a Newtonian plasma. Under physiological conditions ($V_{plate} = 1.3 - 15$ mm/s), our findings reveal that the deformation of the ECs is minimal, but they tend to align in the direction of flow. Although the structural variations of the ECs introduced by their elastic response do not seem to affect the hydrodynamics of the circulating blood plasma under these conditions, the slight variations in the shape characteristics of the representative domain do.

Most of the EC deformation occurs at the top of the cell protrusion, which receives the maximum shearing. The developing shear

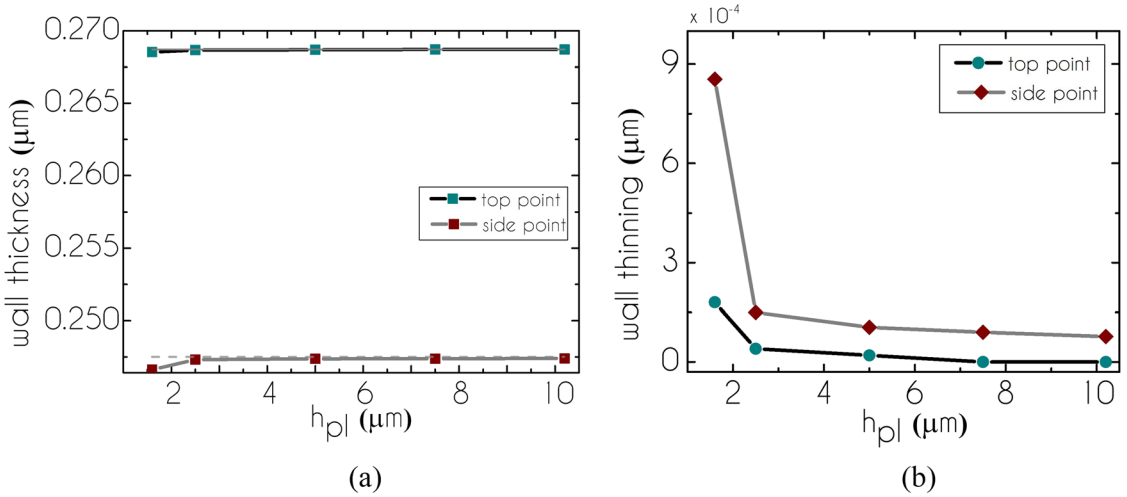

FIG. 18. (a) Wall thickness at the top point of the cell protrusion (point A in Fig. 7) and side point of the flow separation (point B in Fig. 7) for various h_{pl} cases. (b) Wall thinning trends at the two distinct locations for various h_{pl} cases. Dashed line corresponds to the initial thickness of the wall at the side point while the solid line corresponds to the initial thickness of the wall at the top point.

stresses in the plasma region and in the cytoplasmic region portray a linear relation to the imposed top plate velocity under physiological conditions, while in the case of extreme velocities ($V_{plate} = 15 - 350$ mm/s), shear stresses in the cytoplasm increase quadratically with V_{plate}. Stresses, both normal and shear, also develop in the nucleus, indicating that the nucleus does not remain unaffected even under physiological conditions. These stresses increase linearly with increasing V_{plate} and indicate a tendency for rotation of the nucleus. The normal stresses in both the cytoplasmic region and the nucleus are lower when compared to the shear ones, but between them, they have almost the same order of magnitude. They indicate a lateral compression of the cell and the nucleus.

WSS indicates the shearing that the cell membrane receives by the plasma flow and is strongly correlated with wall thinning and possibly to bleb formation. The variation of WSS along the cell wall (−0.57 to 5.1 Pa) is considered significant. Thus, we conclude that an assumption of uniform WSS over the endothelium, as Dabagh *et al.*[63] adopted, would be an oversimplification and would not correspond to true conditions.

Although wall thinning is anticipated at the location of the highest shearing, this is valid under physiological flow conditions, while under extreme shearing conditions, wall thinning is more prevalent at the location of flow stagnation, where extensional forces act upon the cell membrane (Fig. 15). Variation in h_{pl} causes more significant deviation of the wall thickness from its initial value at the point of the flow stagnation, whereas the wall retains its initial thickness at the top point of cell protrusion.

ACKNOWLEDGMENTS

This work is part of the Research Project "Multiscale modeling for the autoregulation of Microvessels, CARE," which was supported by the Hellenic Foundation for Research and Innovation (H.F.R.I.) under the "1st Call for H.F.R.I. Research Projects to support Faculty members and Researchers and the procurement of high-cost research equipment" (Project No. 81105).

AUTHOR DECLARATIONS

Conflict of Interest

The authors have no conflicts to disclose.

Author Contributions

Konstantina Psaraki: Conceptualization (lead); Data curation (lead); Formal analysis (lead); Investigation (lead); Software (lead); Validation (lead); Visualization (lead); Writing – original draft (lead). **Vlasis Mitsoulas:** Formal analysis (supporting); Methodology (supporting); Software (supporting). **Stavros Pavlou:** Conceptualization (supporting); Investigation (supporting); Methodology (supporting); Writing – review & editing (supporting). **Yannis Dimakopoulos:** Funding acquisition (lead); Project administration (lead); Resources (lead); Supervision (lead); Writing – review & editing (supporting).

DATA AVAILABILITY

The data that support the findings of this study are available within the article.

NOMENCLATURE

AFM	Atomic force microscopy
ALE	Arbitrary Lagrangian Eulerian
BSI	Biphasic structure interaction
CAE	Computer-aided engineering
CSK	Cytoskeleton
EC	Endothelial cell
ECM	Endothelial cell monolayer
EVP	Elastoviscoplastic
FEM	Finite element method
FSI	Fluid structure interaction
PDMS	Polydimethylsiloxane
WSS	Wall shear stress

REFERENCES

[1]D. B. Camasão and D. Mantovani, "The mechanical characterization of blood vessels and their substitutes in the continuous quest for physiological-relevant performances. A critical review," Mater. Today Bio **10**, 100106 (2021).
[2]C. Singh, C. S. Wong, and X. Wang, "Medical textiles as vascular implants and their success to mimic natural arteries," J. Funct. Biomater. **6**(3), 500–525 (2015).
[3]C. Michiels, "Endothelial cell functions," J. Cell. Physiol. **196**(3), 430–443 (2003).
[4]M. J. Cipolla, J. Smith, M. M. Kohlmeyer, and J. A. Godfrey, "SKCa and IKCa channels, myogenic tone, and vasodilator responses in middle cerebral arteries and parenchymal arterioles: Effect of ischemia and reperfusion," Stroke **40**(4), 1451–1457 (2009).
[5]M. Félétou, *The Endothelium, Part 1: Multiple Functions of the Endothelial Cells—Focus on Endothelium-Derived Vasoactive Mediators*, 1st ed. (Morgan & Claypool Life Sciences, 2011).
[6]P. F. Davies, "Hemodynamic shear stress and the endothelium in cardiovascular pathophysiology," Nat. Clin. Pract. Cardiovasc. Med. **6**(1), 16–26 (2009).
[7]K. A. Barbee, T. Mundel, R. Lal, and P. F. Davies, "Subcellular distribution of shear stress at the surface of flow-aligned and nonaligned endothelial monolayers," Am. J. Physiol.: Heart Circ. Physiol. **268**(4), H1765–H1772 (1995).
[8]C. F. Dewey, Jr., S. R. Bussolari, M. A. Gimbrone, Jr., and P. F. Davies, "The dynamic response of vascular endothelial cells to fluid shear stress," J. Biomech. Eng. **103**(3), 177–185 (1981).
[9]J. C. Davila, R. J. Rodriguez, R. B. Melchert, and D. Acosta, Jr., "Predictive value of in vitro model systems in toxicology," Annu. Rev. Pharmacol. Toxicol. **38**, 63–96 (1998).
[10]Y. Xia and G. M. Whitesides, "Soft lothography," Annu. Rev. Mater. Sci. **28**(1), 153–184 (1998).
[11]D. Huh, B. D. Matthews, A. Mammoto, M. Montoya-Zavala, H. Y. Hsin, and D. E. Ingber, "Reconstituting organ-level lung functions on a chip," Science **328**(5986), 1662–1668 (2010).
[12]P.-H. Wu, D. R.-B. Aroush, A. Asnacios, W.-C. Chen, M. E. Dokukin, B. L. Doss, *et al.*, "A comparison of methods to assess cell mechanical properties," Nat. Methods **15**(7), 491–498 (2018).
[13]P. Fernández, L. Heymann, A. Ott, N. Aksel, and P. A. Pullarkat, "Shear rheology of a cell monolayer," New J. Phys. **9**(11), 419–419 (2007).
[14]H. Dakhil, D. F. Gilbert, D. Malhotra, A. Limmer, H. Engelhardt, A. Amtmann, J. Hansmann, H. Hübner, R. Buchholz, O. Friedrich, and A. Wierschem, "Measuring average rheological quantities of cell monolayers in the linear viscoelastic regime," Rheol. Acta **55**(7), 527–536 (2016).
[15]K. M. I. Bashir, S. Lee, D. H. Jung, S. K. Basu, M.-G. Cho, and A. Wierschem, "Narrow-gap rheometry: A novel method for measuring cell mechanics," Cells **11**(13), 2010 (2022).
[16]S. G. Eskin, C. L. Ives, L. V. McIntire, and L. T. Navarro, "Response of cultured endothelial cells to steady flow," Microvasc. Res. **28**(1), 87–94 (1984).
[17]N. Kataoka, S. Ujita, and M. Sato, "Effect of flow direction on the morphological responses of cultured bovine aortic endothelial cells," Med. Biol. Eng. Comput. **36**(1), 122–128 (1998).

[18]M. J. Levesque and R. M. Nerem, "The elongation and orientation of cultured endothelial cells in response to shear stress," J. Biomech. Eng. **107**(4), 341 (1985).
[19]P. Dieterich, M. Odenthal-Schnittler, C. Mrowietz, M. Krämer, L. Sasse, H. Oberleithner, and H.-J. Schnittler, "Quantitative morphodynamics of endothelial cells within confluent cultures in response to fluid shear stress," Biophys. J. **79**(3), 1285–1297 (2000).
[20]R. Zakerzadeh, "A computational model for fluid-porous structure interaction," Doctoral dissertation (University of Pittsburgh, 2016).
[21]J. Bear and Y. Bachmat, *Introduction to Modeling of Transport Phenomena in Porous Media* (Springer, 1990).
[22]O. Coussy, *Mechanics of Porous Continua* (Wiley, Chichester, 1995).
[23]S. Whitaker, "The transport equations for multi-phase systems," Chem. Eng. Sci. **28**(1), 139–147 (1973).
[24]W. G. Gray and C. T. Miller, "A generalization of averaging theorems for porous medium analysis," Adv. Water Res. **62**(Part B), 227 (2013).
[25]A.-T. Vuong, C. Ager, and W. A. Wall, "Two finite element approaches for Darcy and Darcy–Brinkman flow through deformable porous media—Mixed method vs. NURBS based (isogeometric) continuity," Comput. Methods Appl. Mech. Eng. **305**, 634–657 (2016).
[26]K. Wang, X. H. Sun, Y. Zhang, T. Zhang, Y. Zheng, Y. C. Wei, P. Zhao, D. Y. Chen, H. A. Wu, W. H. Wang, R. Long, J. B. Wang, and J. Chen, "Characterization of cytoplasmic viscosity of hundreds of single tumor cells based on micropipette aspiration," R. Soc. Open Sci. **6**, 181707 (2019).
[27]Y. Yang and H. Jiang, "Shape and dynamics of adhesive cells: Mechanical response of open systems," Phys. Rev. Lett. **118**(20), 208102 (2017).
[28]A. R. Bausch, W. Möller, and E. Sackmann, "Measurement of local viscoelasticity and forces in living cells by magnetic tweezers," Biophys. J. **76**(1), 573–579 (1999).
[29]L. Preziosi, D. Ambrosi, and C. Verdier, "An elasto-visco-plastic model of cell aggregates," J. Theor. Biol. **262**(1), 35–47 (2010).
[30]T. J. Mitchison, G. T. Charras, and L. Mahadevan, "Implications of a poroelastic cytoplasm for the dynamics of animal cell shape," Semin. Cell Dev. Biol. **19**(3), 215–223 (2008).
[31]N. G. Cogan and R. D. Guy, "Multiphase flow models of biogels from crawling cells to bacterial biofilms," HFSP J. **4**(1), 11–25 (2010).
[32]M. Dembo and F. Harlow, "Cell motion, contractile networks, and the physics of interpenetrating reactive flow," Biophys. J. **50**(1), 109–121 (1986).
[33]R. De Boer, "Highlights in the historical development of the porous media theory: Toward a consistent macroscopic theory," Appl. Mech. Rev. **49**(4), 201 (1996).
[34]A. Malandrino and E. Moeendarbary, "Poroelasticity of living tissues," in *Encyclopedia of Biomedical Engineering*, edited by R. Narayan (Elsevier, 2019), pp. 238–245, available at https://www.sciencedirect.com/science/article/pii/B978012801238399932X?via%3Dihub.
[35]A. E. Ehret, K. Bircher, A. Stracuzzi, V. Marina, M. Zündel, and E. Mazza, "Inverse poroelasticity as a fundamental mechanism in biomechanics and mechanobiology," Nat. Commun. **8**(1), 1002 (2017).
[36]W. Strychalski and R. D. Guy, "Intracellular pressure dynamics in blebbing cells," Biophys. J. **110**(5), 1168–1179 (2016).
[37]E. Moeendarbary, L. Valon, M. Fritzsche, A. R. Harris, D. A. Moulding, A. J. Thrasher, E. Stride, L. Mahadevan, and G. T. Charras, "The cytoplasm of living cells behaves as a poroelastic material," Nat. Mater. **12**(3), 253–261 (2013).
[38]W. Jung, J. Li, O. Chaudhuri, and T. Kim, "Nonlinear elastic and inelastic properties of cells," J. Biomech. Eng. **142**(10), 100806 (2020).
[39]J. S. Bois, F. Jülicher, and S. W. Grill, "Pattern formation in active fluids," Phys. Rev. Lett. **106**(2), 028103 (2011).
[40]M. Radszuweit, S. Alonso, H. Engel, and M. Bär, "Intracellular mechanochemical waves in an active poroelastic model," Phys. Rev. Lett. **110**, 138102 (2013).
[41]M. Dabagh, P. Jalali, P. J. Butler, A. Randles, and J. M. Tarbell, "Mechanotransmission in endothelial cells subjected to oscillatory and multidirectional shear flow," J. R. Soc., Interface **14**(130), 20170185 (2017).
[42]R. Milo and R. Phillips, *Cell Biology by the Numbers*, 1st ed. (Garland Science, 2015).
[43]K. Giannokostas, Y. Dimakopoulos, A. Anayiotos, and J. Tsamopoulos, "Advanced constitutive modeling of the thixotropic elasto-visco-plastic behavior of blood: Steady-state blood flow in microtubes," Materials **14**(2), 367 (2021).
[44]H. Sarin, "Physiologic upper limits of pore size of different blood capillary types and another perspective on the dual pore theory of microvascular permeability," J. Angiog. Res. **2**(1), 14 (2010).
[45]M. A. Klausner, L. J. Hirsch, P. F. Leblond, J. K. Chamberlain, M. R. Klemperer, and G. B. Segel, "Contrasting splenic mechanisms in the blood clearance of red blood cells and colloidal particles," Blood **46**(6), 965–976 (1975).
[46]H. Fischer, I. Polikarpov, and A. F. Craievich, "Average protein density is a molecular-weight-dependent function," Protein Sci. **13**(10), 2825–2828 (2004).
[47]R. L. Satcher and C. F. Dewey, "Theoretical estimates of mechanical properties of the endothelial cell cytoskeleton," Biophys. J. **71**(1), 109–118 (1996).
[48]N. Caille, O. Thoumine, Y. Tardy, and J. J. Meister, "Contribution of the nucleus to the mechanical properties of endothelial cells," J. Biomech. **35**(2), 177–187 (2002).
[49]R. Vargas-Pinto, H. Gong, A. Vahabikashi, and M. Johnson, "The effect of the endothelial cell cortex on atomic force microscopy measurements," Biophys. J. **105**(2), 300–309 (2013).
[50]B. Martinac, Y. A. Nikolaev, G. Silvani, N. Bavi, V. Romanov, Y. Nakayama, A. D. Martinac, P. Rohde, O. Bavi, and C. D. Cox, "Cell membrane mechanics and mechanosensory transduction," Curr. Top. Membr. **86**, 83–141 (2020).
[51]M. Brust, C. Schaefer, R. Doerr, L. Pan, M. Garcia, P. E. Arratia, and C. Wagner, "Rheology of human blood plasma: Viscoelastic versus Newtonian behavior," Phys. Rev. Lett. **110**(7), 078305 (2013).
[52]V. Mitsoulas, S. Varchanis, Y. Dimakopoulos, and J. Tsamopoulos, "Dynamics and apparent permeability of the glycocalyx layer: Start-up and pulsating shear experiments *in silico*," Phys. Rev. Fluids **7**, 013102 (2022).
[53]K. Giannokostas, D. Photeinos, Y. Dimakopoulos, and J. Tsamopoulos, "Quantifying the non-Newtonian effects of pulsatile hemodynamics in tubes," J. Non-Newtonian Fluid Mech. **298**, 104673 (2021).
[54]K. Giannokostas, Y. Dimakopoulos, and J. Tsamopoulos, "Shear stress and intravascular pressure effects on vascular dynamics: Two-phase blood flow in elastic microvessels accounting for the passive stresses," Biomech. Model. Mechanobiol. **21**, 1659–1684 (2022).
[55]M. E. Levenston, E. H. Frank, and A. J. Grodzinsky, "Variationally derived 3-field finite element formulations for quasistatic poroelastic analysis of hydrated biological tissues," Comput. Methods Appl. Mech. Eng. **156**(1–4), 231–246 (1998).
[56]R. E. Goldstein, "*Batchelor Prize Lecture* Fluid dynamics at the scale of the cell," J. Fluid Mech. **807**, 1–39 (2016).
[57]A. Mogilner and A. Manhart, "Intracellular fluid mechanics: Coupling cytoplasmic flow with active cytoskeletal gel," Annu. Rev. Fluid Mech. **50**(1), 347–370 (2018).
[58]W. Strychalski, C. A. Copos, O. L. Lewis, and R. D. Guy, "A poroelastic immersed boundary method with applications to cell biology," J. Comput. Phys. **282**, 77–97 (2015).
[59]C. Ager, B. Schott, M. Winter, and W. A. Wall, "A Nitsche-based cut finite element method for the coupling of incompressible fluid flow with poroelasticity," Comput. Methods Appl. Mech. Eng. **351**, 253–280 (2019).
[60]D. Yuan, S. M. Somers, W. L. Grayson, and A. A. Spector, "A poroelastic model of a fibrous-porous tissue engineering scaffold," Sci. Rep. **8**(1), 5043 (2018).
[61]SALOME, see http://www.salome-platform.org/ for "The open source integration platform for numerical simulation."
[62]Y. Wang and P. Dimitrakopoulos, "Nature of the hemodynamic forces exerted on vascular endothelial cells or leukocytes adhering to the surface of blood vessels," Phys. Fluids **18**(8), 087107 (2006).
[63]M. Dabagh, P. Jalali, P. J. Butler, and J. M. Tarbell, "Shear-induced force transmission in a multicomponent, multicell model of the endothelium," J. R. Soc. Interface **11**(98), 20140431 (2014).
[64]M. Sato and N. Ohshima, "Effect of wall shear rate on thrombogenesis in microvessels of the rat mesentery," Circulation Res. **66**(4), 941–949 (1990).
[65]J.-O. Fortrat, T. Levrard, S. Courcinous, and J. Victor, "Self-organization of blood pressure regulation: Experimental evidence," Front. Physiol. **7**, 112 (2016).
[66]N. Resnick, H. Yahav, L. M. Khachigian, T. Collins, K. R. Anderson, F. C. Dewey, and M. A. Gimbrone, Jr., "Endothelial gene regulation by laminar shear stress," Adv. Exp. Med. Biol. **430**, 155–164 (1997).